bioRxiv preprint doi: https://doi.org/10.1101/199778; this version posted October 17, 2017. The copyright holder for this preprint (which was not certified by peer review) is the author/funder, who has granted bioRxiv a license to display the preprint in perpetuity. It is made available under aCC-BY-NC-ND 4.0 International license.

Visualizing intricate acto-myosin dynamics at a membrane surface using interferometric scattering microscopy

Darius Köster[1,2,*] Nikolas Hundt[3], Gavin Young[3], Adam Fineberg[3], Philipp Kukura[3], Satyajit Mayor[1,4]

1 National Centre for Biological Sciences, Tata Institute for Fundamental Research, GKVK, Bellary Road, Bangalore, 560065, India
2 Division of Biomedical Sciences, Warwick Medical School, University of Warwick, Coventry CV4 7AL, UK
3 Physical and Theoretical Chemistry Laboratory, Department of Chemistry, University of Oxford, South Parks Road, Oxford OX1 3QZ, UK
4 Institute for Stem Cell Biology and Regenerative Medicine, Bangalore 560065, India
* corresponding author: d.koester@warwick.ac.uk

Abstract

The surface of mammalian cells, i.e. the plasma membrane and the underlying cytoskeletal cortex, constitutes an active platform for many cellular processes including cargo uptake, signaling and formation of cell adhesions. Experimental and theoretical work has recently shown that acto-myosin dynamics can modify the local membrane organization, but the molecular details are not well understood. Here, we use interferometric scattering (iSCAT) microscopy to investigate a minimal acto-myosin network linked to a supported lipid bilayer. We demonstrate that we are able to detect and distinguish actin and myosin filaments label-free based on their interferometric scattering contrast. The scattering-based approach allows us to follow diffusion of single actin filaments attached to the bilayer at high frame rates revealing different types of diffusion depending on filament length. We investigate the directed motion of myosin II filaments on the actin network quantifying binding kinetics and processivity at varying ATP concentrations. Finally, we follow long-term network flow and organization enabling us to compare our observations with theoretical models of network dynamics. Our results demonstrate that iSCAT microscopy is an ideal tool to investigate multi-component systems on a broad range of length scales, resolving molecular scale mechanisms such as single myosin filament dynamics as well as acto-myosin network contraction on the mesoscopic scale.

Introduction

The acto-myosin cortex in living cells is necessary for the mechanical stability of the cell and influences the organization of the adjacent plasma membrane. Several studies have shown that the cell cortex influences the dynamics and mobility of particular membrane components (1–3) and there is increasing evidence that the dynamic remodeling of the acto-myosin network drives the local concentration and clustering of membrane molecules (4–7). The complexity of the acto-myosin cortex and the plasma membrane in live cells makes it difficult to study the molecular details of cortex-membrane interactions and to uncover the underlying mechanisms.

Reconstituted minimal systems provide a tractable way to studying the dynamics of a two-dimensional, membrane bound acto-myosin network, in which fluorescently labeled proteins are dynamically visualized using confocal or total internal reflection fluorescence (TIRF) microscopy (8–11). To capture the full dynamics of the acto-myosin network and to span the temporal range from fast single molecule interactions to long-term network deformations, it is necessary to visualize the network components

bioRxiv preprint doi: https://doi.org/10.1101/199778; this version posted October 17, 2017. The copyright holder for this preprint (which was not certified by peer review) is the author/funder, who has granted bioRxiv a license to display the preprint in perpetuity. It is made available under aCC-BY-NC-ND 4.0 International license.

with a sub-second time-resolution over timescales of tens of minutes. This is difficult to achieve with fluorescent probes due to photo-bleaching and photo-toxicity.

To overcome these limitations, we employed interferometric scattering (iSCAT) microscopy (12), a label free imaging technique that relies on the interference of the light scattered from nano-objects near a glass water interface with the light reflected by the same interface. The key advantage of light scattering over fluorescence detection is the lack of an upper limit to fluorescence emission rate and the absence of photobleaching, enabling long observation times at high-speed acquisition rates (> 1kHz) limited almost exclusively by the camera acquisition speed. Under ideal experimental conditions, shot noise-induced fluctuations of the detected light intensity are the dominant noise source. This results in the iSCAT signal-to-noise ratio scaling with the square root of the detected light intensity, thus effectively limiting the detection sensitivity of the experiment to the incident laser power (12).

Here, we employ iSCAT microscopy for the first time to visualize membrane bound dynamic acto-myosin networks for tens of minutes with sub second frame rates. We characterize actin filament dynamics and myosin II filament attachment times on sub-second time scales, while at the same time observing the large-scale network deformations and remodeling that occur over minutes. Access to this wide range of time-scales will lead to a better understanding of the mechanics and dynamics on the molecular scale and how they translate into network dynamics on a mesoscopic scale. We demonstrate the potential of iSCAT microscopy to observe the intricate dynamics of two-dimensional active networks, providing a valuable addition to existing microscopy tools.

Results

We used iSCAT microscopy set-ups equipped with lasers of either 635nm or 445nm wavelength, to visualize thin films of acto-myosin networks bound via a deca His-SNAP-Ezrin actin binding domain fusion protein (HSE) to supported lipid bilayers containing 98%$_{mol}$ Dioleoyl-phosphocholine (DOPC) and 2%$_{mol}$ 1,2-dioleoyl-sn-glycero-3-[(N-(5-amino-1-carboxypentyl)iminodiacetic acid)succinyl] (nickel salt) (Ni-NTA-DGS) as described earlier (11)(Fig. 1A). Due to the absence of any crowding factors or excess proteins, the actin and myosin II filaments were the principal sources of light scattering and could be clearly discerned using iSCAT microscopy (Fig. 1B, C). The contrast for actin filaments and myosin II filaments was about 20 times stronger when using the 445nm laser iSCAT setup compared to the 635nm laser set up (Sup Fig. 1A, B).

Single filament dynamics in a static actin meshwork

Using the 445nm laser setup to record a membrane bound actin network, we visualized and studied the dynamics of short actin filaments within a network in the absence of myosin motors. To remove any signal originating from static structures such as immobile actin filaments or small impurities in the supported lipid bilayer (SLB), the image sequences were median filtered as described earlier (12) to reveal the mobile elements (Fig. 2A). When we tracked the consecutive landing of actin filaments at the same diffraction-limited spot the interferometric signal increased in a step-wise manner (SupFig2 A,B; Video 1). This suggests that the iSCAT signal grows proportionally with the amount of protein in the region of interest

bioRxiv preprint doi: https://doi.org/10.1101/199778; this version posted October 17, 2017. The copyright holder for this preprint (which was not certified by peer review) is the author/funder, who has granted bioRxiv a license to display the preprint in perpetuity. It is made available under aCC-BY-NC-ND 4.0 International license.

and that the signal can be directly translated into the number of actin filaments stacked on top of each other. Performing this analysis on images showing dense actin networks reveals that in the conditions used here ([actin] = 100-350nM), the actin layer comprises 1 to 6 filaments with most of the regions showing a layer of 2 filaments (Fig. 2B). The characteristic contrast profile of single actin filaments with constructive and destructive interference along the edge and center, respectively, was used to identify and track the filament shape (see methods), its center of mass as well as its orientation (Fig. 2C, D; Video 2). Because we were able to follow the same filament at high frame rates for minutes, we could calculate the mean square displacement of the center of mass (MSD_{CM}) (Fig 2E). The MSD_{CM} ranging over three orders of magnitude in time indicate free diffusion of the short actin filaments within the actin network (Fig 2E). Longer filaments (> 2µm) display a more restricted mobility with a more persistent orientation and a MSD trace that indicates confined diffusion (SupFig. 2 C,D).

iSCAT microscopy reveals binding dynamics of myosin II filaments to actin

We next characterize the dynamics of myosin II filaments interacting with the membrane bound actin filament network. First, we established that our myosin II filaments have a characteristic length of 533(±113) nm (445nm laser) and 556 (±115) nm (635 nm laser) (SupFig. 1C-F), respectively. This is in good agreement with previous measures of muscle myosin II filament length (10).

Second, we analyzed the binding/ unbinding dynamics of myosin II filaments to membrane bound actin filaments in the presence of ATP using the 635nm laser iSCAT setup. These dynamics cannot be easily described by models for the interaction between actin filaments and a single myosin motor domain. Since many myosin heads are neighboring each other in a myosin filament, the filament's movement will depend on the duty cycle of the single myosin heads as well as cooperative effects between heads. Even though individual myosin II motors will not move processively on actin, the concerted action of many motors may lead to processive motion of the myosin filament.(13–16). In addition, myosin filaments exert forces on the actin filaments leading to actin filament motion, rupture or contraction of crosslinked actin filaments (10, 11). Imaging with 5-10Hz for several minutes was sufficient to capture a broad range of myosin filament dynamics with high accuracy (Video 3). To remove any signal originating from static structures such as immobile actin filaments or small impurities in the SLB, the image sequences were median filtered (12). In a second step, a maximum projection of the time series was used to visualize the tracks occupied by myosin II filaments during the experiment. Lines following these tracks were then used to compute kymographs depicting the myosin II filament binding times and their motion along actin filaments (Fig 3A).

At an ATP concentration of 100 µM, myosin II-actin attachment times are widely spread following a double exponential decay with time constants of τ_{off1} = 1.6 (±0.1) s and τ_{off2} = 10 (±3) s and the majority of the events being described by the short attachment time (Fig. 3B). At 10 µM ATP, the system becomes contractile and exhibits large scale contractions (Video 4)(11, 17); correspondingly, the myosin II filament attachment times follow a double exponential decay with time constants of τ_{off1} = 2.1 (±0.4) s and τ_{off2} = 6.4 (±0.9) s and the majority of the events being described by the long attachment time (Fig. 3C). Further analysis of the tracks in the kymographs reveal the differences in the dynamic properties of myosin II filament at high and low ATP concentrations. At 100 µM, the mobile myosin II filaments travel with an average of $v_{myoII\ filament}$ = 0.17 (±0.20) µm s^{-1}, the run length (processivity) distribution decays exponentially with a characteristic run length of λ=0.30 (±0.03) µm (Fig. 3 D, E). Plotting run length versus attachment time shows a weak positive correlation with the short time population showing movement

bioRxiv preprint doi: https://doi.org/10.1101/199778; this version posted October 17, 2017. The copyright holder for this preprint (which was not certified by peer review) is the author/funder, who has granted bioRxiv a license to display the preprint in perpetuity. It is made available under aCC-BY-NC-ND 4.0 International license.

of several micro meters and a population of long attachment times showing short run lengths (Fig 3F). At 10 µM ATP, when the network becomes contractile and the myosin II filament attachment times longer, the mobile myosin II filaments travel with an average velocity of $v_{myoII\ filament}$ = 0.37 (±0.25) µm s^{-1}, the characteristic run length is λ=1.09 (±0.06) µm and the correlation between run length and attachment times is stronger with a majority of myosin II filaments showing persistent movement for several seconds and again a long attachment time population with little movement (Fig 3G-I). It is interesting to note that myosin II filaments move faster and for longer times at low ATP concentrations as a result of the slower unbinding dynamics of individual myosin heads at limited ATP levels. These features of single myosin II filament dynamics could serve as a molecular explanation for the large-scale contraction observed at low ATP levels.

Characterization of acto-myosin network dynamics

Turning to the full network dynamics, we focused on two states of the acto-myosin network, namely the contractile network at 10 µM ATP concentration and the remodeling state at 100 µM ATP concentration as described earlier (11). Since long-term imaging did neither affect the activity of myosin filaments nor the integrity of actin filaments, we were able to observe the transition starting with a homogeneous network, followed by the formation of small clusters and ending by large cluster formation (Fig. 4A, Video 4). We quantified the changes in cluster length scales by computing the density-density autocorrelation function at each time-point, which indicates that clustering sets in after 700s of remodeling and then proceeds continuously into larger scales (Fig. 4B).

The frame rate of 10 Hz enabled us to use particle image velocimetry (PIV) to analyze the myosin II generated flows of the acto-myosin network in the remodeling and contractile states, respectively. The resulting vector fields accounting for the flow velocities can be used to compute the local divergence and reveal the contractile regions (negative divergence) of the acto-myosin network in the contractile state (Fig. 4 C,D). To compare the network dynamics in the contractile versus the remodeling state, we computed the network velocity distribution in both conditions (Fig. 4E). As expected, the network velocities are higher in the contractile state with the mean velocity $v_{network}$ = 74 (±64) nm, whereas $v_{network}$ = 14 (±14) nm in the remodeling state. This result correlates with our observations on myosin II dynamics. Short interaction times of myosin with actin at 100 µM ATP lead to slow displacement of the network in the remodeling state (Fig. 3 B). By contrast, longer interaction times, more persistent and faster displacement of actin filaments by the myosin at 10 µM ATP correspond to faster network velocities in the contractile state (Fig. 3C, E, H).

Sustained vortex formation by the acto-myosin network

Remarkably, we observed the formation of spirals and vortices of the acto-myosin network at low ATP concentrations in some of our experiments (Fig. 4F, Video 5). These vortices typically comprised multiple myosin II filaments moving around a common central point. They had a radius of 1-5 µm and were stable for several minutes. PIV on single vortices showed a general circular flow around the center with a velocity profile that peaks at about half of the vortex radius (Fig. 4G, H), which is in good agreement with earlier theoretical work (18, 19). Although vortex formation is expected for active gels of polar filaments, it was experimentally realized and described in microtubule networks, but, to our knowledge, not yet in acto-myosin networks.

bioRxiv preprint doi: https://doi.org/10.1101/199778; this version posted October 17, 2017. The copyright holder for this preprint (which was not certified by peer review) is the author/funder, who has granted bioRxiv a license to display the preprint in perpetuity. It is made available under aCC-BY-NC-ND 4.0 International license.

Discussion

Here we demonstrate how iSCAT microscopy can be used to observe complex, multi component systems such as lipid membrane anchored acto-myosin networks. The key advantages of iScat are: (i) label-free imaging, (ii) acquisition rates up-to the kHz range, limited only by laser intensity and camera acquisition rates, and (iii) selective resolving of system components by varying incident laser wavelength (e.g. actin filaments are clearly visualized at 445nm, but not at 635nm). For these reasons, we expect iSCAT microscopy to be useful in the study of reconstituted systems, complementing fluorescence-based approaches (12).

In this work, we used the high temporal resolution of iScat to track the position and shape of individual actin filaments over long time periods, facilitated by the absence of photo damage and long imaging times; we were able to do so over several orders of magnitude in the time domain (0.1-1000 s).This opens up the possibility of a more detailed examination of the motion of filaments within complex networks, suitable for comparison with physical theory (20, 21)

The study of myosin II filament dynamics on an actin filament inside the membrane bound, remodeling acto-myosin network provides new insights into the physico-chemical properties of a myosin ensemble in relation to network dynamics.Interestingly, we found a regime in which the myosin filament velocity increases with decreasing ATP concentrations. This is in agreement with a recent theoretical study of myosin filament dynamics, that has proposed this behavior for muscle myosin filaments when the ATP concentrations are 100 µM and lower and the mechanical load is low (16). Correspondingly, our measurements on the myosin filament velocities match the velocities estimated for the relevant ATP concentrations (16). This study and our experimental observations demonstrate how minute changes in the single myosin head domain properties (due to changing ATP concentration) can lead to big, and non-trivial, differences in the properties of myosin filaments.

The dynamics of myosin filaments were found to have consequences on the whole acto-myosin network. Short attachment times of myosin filaments limit the persistence of myosin motion, as well as the number of actin filaments that are crosslinked by myosin filaments. In this regime, the action of a single myosin filament is local, and the acto-myosin network is in a locally remodeling/fluctuating state without large-scale contraction. In contrast, long attachment times and persistent motion of myosin filaments increase the connectivity of the acto-myosin network and promote the transmission of stresses over longer distances, leading to a switch from a locally remodeling to a globally contractile state (22).

In addition our iSCAT studies reveal two populations of myosin II filament attachment times. One with short attachment times in the range of 2 s and one with very long attachment times described by a characteristic attachment time of 6-10s. Compared to the binding time of a single myosin head domain of 25-40 ms, the observed attachment times represent binding of multiple myosin head domains (16, 23). It remains to be elucidated what the nature of the two attachment time populations is. The head domains in a myosin II filaments are arranged in a dumbbell structure, i.e. both ends being enriched with myosin heads and a thin, bare stalk in the middle. One possibility is that the short attachment regime represents attachments to an actin filament with multiple heads of one filament side. The longer attachment regime might then represent myosin filaments that bind actin filaments with both sides. The observation that many of the myosin II filaments with long attachment times show only little motion might indicate binding of the myosin filament to two, anti-parallel oriented actin filaments resulting in

bioRxiv preprint doi: https://doi.org/10.1101/199778; this version posted October 17, 2017. The copyright holder for this preprint (which was not certified by peer review) is the author/funder, who has granted bioRxiv a license to display the preprint in perpetuity. It is made available under aCC-BY-NC-ND 4.0 International license.

the stall of the myosin motion (Fig. 5). In the future, more detailed studies using non-muscle myosin II isoforms which allow tight control of the number of functional head domains (24) will be ideal to test the nature of the longer binding times as well as the theoretically predicted differences at low ATP concentrations between muscle and non-muscle myosin II filaments (16).

Further, the ability to follow all network components over a long time with high temporal resolution allows one to relate individual myosin II filament dynamics with the local activity and stresses transmitted to the actin network, e.g. as monitored by the application of PIV. We show that PIV reveals regions of negative divergence in the acto-myosin flow fields characteristic of contractile networks (18, 25). Interestingly, these contractile regions are stable over time scales of hundreds of seconds and seem to constitute a steady state where myosin II filaments continue to travel towards existing myosin clusters and detach before getting jammed in the cluster. The observation of vortices represents another active steady state that was predicted in a theoretical work on active gels by Kruse and colleagues (18). It is exciting that these structures, which were observed recently in live cells (26), could now be realized for the first time in a reconstituted system. It is likely that earlier studies simply did not employ the right concentration of actin and myosin to foster vortex formation, or that the ability to observe the system for longer times without any photodamage favored vortices. However, more detailed studies will be needed to understand, why such structures were not reported earlier. Exploring the network dynamics and its contractile behavior as a function of actin, myosin and ATP concentration, and to compare this with theoretical predictions will be of interest to gain deep insights into such active systems. iSCAT microscopy will be a valuable tool in this endeavor.

Materials and Methods

Purified Proteins

Actin was purified from chicken breast following the protocol from Spudich and Watt (27) and kept on ice in monomeric form in G-buffer (2 mM Tris Base, 0.2 mM ATP, 0.5 mM TCEP-HCl, 0.04% NaN_3, 0.1 mM CaCl2, pH 7.0); Myosin II was obtained from chicken breast following a modified protocol from Pollard (28) and kept in monomeric form in myo-buffer (500 mM KCl, 1 mM EDTA, 1 mM DTT, 10 mM HEPES, pH 7.0). The day prior to experiments, functional myosin II proteins are separated from proteins containing dead head domains by a round of binding and unbinding to F-actin at a 5:1 actin to myosin ratio (switch from no ATP to 3 mM ATP) followed by a spin at 60000 rpm for 10 min at 4^{o}C in a TLA100.3 rotor. The supernatant containing functional myosin II is dialyzed against myo-buffer over-night and used for experiments for up to three days.

To link actin to the SLB, we used a construct containing 10x His domains followed by a linker (KCK) and the actin binding domain of Ezrin as described earlier (11)

Supported Lipid Bilayer and Experimental Chamber Preparation

Glass coverslips (#1.5 borosilicate, Menzel, Germany) for SLB formation were cleaned with Hellmanex III (Hellma Analytics, Mühleim, Germany) following the manufacturer's instructions followed by thorough rinses with EtOH and MilliQ water, blow dried with N2 and finally passed briefly over a Bunsen burner flame. For the experimental chamber, 0.2 ml PCR tubes (Tarsons Products, Kolkata, India) were cut to

bioRxiv preprint doi: https://doi.org/10.1101/199778; this version posted October 17, 2017. The copyright holder for this preprint (which was not certified by peer review) is the author/funder, who has granted bioRxiv a license to display the preprint in perpetuity. It is made available under aCC-BY-NC-ND 4.0 International license.

remove the lid and the conical bottom part and stuck to the cleaned glass using UV glue (NOA88, Norland Products, Cranbury, NJ) and three minutes curing by intense UV light at 365nm (PSD-UV8T, Novascan, Ames, IA). Freshly cleaned and assembled chambers were directly used for experiments.

Supported lipid bilayers (SLB) were formed by fusion of small uni-lamellar vesicles (SUV). Lipid mixtures containing 98% DOPC and 2% DGS-NTA(Ni2+) were mixed together with 1ml chloroform (Electron Microscopy Sciences, Hatfield, PA) in a cleaned amber glass vial (B7990-2A, Thermo Fisher Scientific, Rockwood, TN), dried under a N2 stream, placed in a vacuum desiccator overnight and resuspended in SUV storage buffer (150 mM NaCl, 20 mM HEPES, 5% sucrose, pH 7.2) to a final lipid concentration of 4 mM. SUVs of ~80 nm diameter were formed by the extrusion method using a lipid extruder (Avanti Polar Lipids Inc.) with an 80 nm pore size polycarbonate filter membrane (GE Whatman, Piscataway, NJ).

For SLB formation, 10-20 µl of SUV mix were added to 100 µl of SLB formation buffer (150 mM NaCl, 2 mM CaCl2, 20 mM Hepes, pH 5.5), incubated for 20 min at RT and washed ten times with SLB working buffer (150 mM NaCl, 20 mM HEPES, 0.1 mg/ml β-casein, pH 7.2). For experiments with F-actin, SLB working buffer was replaced by 100 µl KMEH (50 mM KCl, 2 mM MgCl2, 1 mM EGTA, 20 mM HepesHEPES, pH 7.2).

Formation of Acto-Myosin Network

In a typical experiment, 10 nM HKE were added to SLBs and incubated for 40min followed by three washes with KMEH. During this incubation time, F-actin was polymerized by addition of $10\%_{vol}$ of 10x ME buffer (100 mM MgCl2, 20 mM EGTA, pH 7.2) to the G-actin stock and 2min incubation to replace G-actin bound Ca^{2+} ions with Mg^{2+}. Polymerization buffer was added to induce F-actin polymerization in a test tube at a final G-actin concentration of 5 µM in KMEH supplemented with 2 mM ATP. After 20-30 min incubation, the desired amount of F-actin was added to the SLBs using blunt cut 200 µl pipette tips. An incubation of 30 min allowed the F-actin layer to bind to the SLB at steady state, myosin II filaments were added afterwards and the evolution of the acto-myosin system was observed for up to 90 min. To induce remodelling of the acto-myosin system, Mg-ATP (100 mM) was added to a final concentration of 1 mM. Each step of this procedure was performed on the microscope stage, which allowed us to check its state continuously. The open chamber design allowed the addition of each component from top without induction of flows that would perturb the actin network.

iSCAT microscopes

Interferometric scattering microscopy was performed on two different home-built setups similar to those detailed in (29, 30). Briefly, a weakly focused laser beam was scanned across the sample over an area of 24 x 24 μm^2 (445 nm laser) or 32.6 x 32.6 μm^2 (635 nm laser). The light reflected from the glass-water interface together with the scattered light from the sample was imaged onto a CMOS camera (445 nm laser: Point Grey GS3-U3-23S6M-C, Flir, Canada; 635 nm laser: MV-D1024-160-CL-8, Photonfocus, Switzerland). The cameras were controlled using home-written Labview software. The setup with the 445 nm laser had a 3.5 mm partially reflective mirror placed in the re-imaged back focal plane of the objective for enhanced scattering contrast as described in(30). The videos were recorded at 10 fps (445 nm laser) and 5 fps (635 nm laser) with the illumination intensity on the sample (445 nm laser: 250

bioRxiv preprint doi: https://doi.org/10.1101/199778; this version posted October 17, 2017. The copyright holder for this preprint (which was not certified by peer review) is the author/funder, who has granted bioRxiv a license to display the preprint in perpetuity. It is made available under aCC-BY-NC-ND 4.0 International license.

W/cm2; 635 nm laser: 1.9 kW/cm2) set to nearly saturate the camera with the returning light. The pixel sizes were 23.4 nm/pixel (445 nm laser) and 31.8 nm/pixel (635 nm laser).

Image processing

Non-sample specific illumination inhomogeneities, fixed-pattern noise and constant background were removed from the raw images by dividing each of them with a flat field image that contained only these features. The flat field image was computed by recording 2000 frames of the sample while moving the stage. For each pixel, a temporal median was calculated resulting in a flat field image that only contained static features.

Median filtering

Movies were median filtered using Matlab (MathWorks, Natick, MA, USA). For each image sequence, the median is computed for each pixel, deleted from the original image sequence and the median filtered image sequence as well as the computed median filter are saved.

Actin filament tracking

Actin filaments that became visible after median filtering and that did not cross other actin filaments for at least 1000 frames were tracked using image J (http://imagej.nih.gov) and the plugin JFilament (http://athena.physics.lehigh.edu/jfilament). The obtained tracking traces were analyzed using Matlab to compute the position of the center of mass (CM) for each time point and to generate plots of the CMs mean square displacement.

Myosin length measurements

Intensity line-scans along the long axis of single myosin filaments were taken and the distance between the half maximum points at both ends were taken as the length of the myosin II filament.

Myosin binding dynamics

Median filtered image sequences were inverted, from which maximum projections were generated to reveal regions of myosin II filament binding (i.e. actin filaments). Lines were drawn along those regions and used to generate kymographs (kymograph tool in Image J, line width 3), which were analyzed afterwards manually to measure binding times and run lengths. The resulting velocity distribution, run length distribution and correlation between run length and bound time were plotted using OriginPro 2016 (OriginLab Corporation, Northampton, MA, USA).

Particle Image Velocimetry

Particle Image Velocimetry (PIV) was performed using PIVlab (31, 32) (Garcia, D. (2011): A fast all-in-one method for automated post-processing of PIV data. Experiments in Fluids, Springer-Verlag, 2011, 50,

bioRxiv preprint doi: https://doi.org/10.1101/199778; this version posted October 17, 2017. The copyright holder for this preprint (which was not certified by peer review) is the author/funder, who has granted bioRxiv a license to display the preprint in perpetuity. It is made available under aCC-BY-NC-ND 4.0 International license.

1247-1259). Median filtered image sequences were inverted and transformed into 8-bit format using Image J. The PIV vector maps were computed with the FFT window deformation algorithm and the window sizes of 64, 32 and 16 pixels and step sizes of 32, 16 and 8 pixels, respectively. The accepted range of velocity vectors was limited to ± 2 µm s^{-1}. *Intensity autocorrelation*

Image sequences were inverted before the intensity autocorrelation, $\chi(\vec{x}) = < \delta_I(\vec{y})\ \delta_I(\vec{y}+\vec{x}) >$ $\chi(\vec{x}) = < \delta_I(\vec{y})\ \delta_I(\vec{y}+\vec{x}) >$, was computed in Matlab with a fast Fourier transform and summed over the angular coordinate to obtain χ(r).

Contributions:

DK conceived, designed and performed experiments, analyzed data, wrote manuscript; NH helped in the experiments, analyzed data, wrote manuscript; GY and AF did set up the iSCAT microscopes; PK conceived experiments, wrote manuscript; SM conceived experiments wrote manuscript.

Acknowledgements

DK thanks Madan Rao and Kabir Husain (NCBS) for instructive discussions and comments on the manuscript and the Company of Biologists for supporting this work with a Travelling fellowship. NH thanks James Sellers and Yasuharu Takagi from the NIH for providing the actin. DK was supported by a postdoctoral fellowship of NCBS; NH was supported by DFG research fellowship, grant HU 2462/1-1. GY was supported by a Zvi and Ofra Meitar Magdalen Graduate Scholarship; PK was supported by an ERC Starting Investigator Grant (Nanoscope, 337577); SM is supported by a JC Bose Fellowship from the Department of Science and Technology, a Margadarshi Fellowship IA/M/15/1/502018 (Wellcome Trust–Department of Biotechnology, India Alliance), from the Government of India.

References:

1. Kusumi, A., C. Nakada, K. Ritchie, K. Murase, K. Suzuki, H. Murakoshi, R.S. Kasai, J. Kondo, T. Fujiwara, and HidejiMurakoshi. 2005. Paradigm shift of the plasma membrane concept from the two-dimensional continuum fluid to the partitioned fluid: high-speed single-molecule tracking of membrane molecules. Annu. Rev. Biophys. Biomol. Struct. 34: 351–78.

2. Arumugam, S., and P. Bassereau. 2015. Membrane nanodomains: contribution of curvature and interaction with proteins and cytoskeleton. Essays Biochem. 57: 109–19.

3. Saka, S.K., A. Honigmann, C. Eggeling, S.W. Hell, T. Lang, and S.O. Rizzoli. 2014. Multi-protein assemblies underlie the mesoscale organization of the plasma membrane. Nat. Commun. 5: 1–14.

4. Rao, M., and S. Mayor. 2014. Active organization of membrane constituents in living cells. Curr. Opin. Cell Biol. 29C: 126–132.

5. van Zanten, T.S., A. Cambi, M. Koopman, B. Joosten, C.G. Figdor, M.F. Garcia-Parajo, and T.S. Van Zanten. 2009. Hotspots of GPI-anchored proteins and integrin nanoclusters function as nucleation sites for cell adhesion. Proc. Natl. Acad. Sci. U. S. A. 106: 18557–62.

bioRxiv preprint doi: https://doi.org/10.1101/199778; this version posted October 17, 2017. The copyright holder for this preprint (which was not certified by peer review) is the author/funder, who has granted bioRxiv a license to display the preprint in perpetuity. It is made available under aCC-BY-NC-ND 4.0 International license.

6. Plowman, S.J., C. Muncke, R.G. Parton, and J.F. Hancock. 2005. H-ras, K-ras, and inner plasma membrane raft proteins operate in nanoclusters with differential dependence on the actin cytoskeleton. Proc. Natl. Acad. Sci. U. S. A. 102: 15500–5.

7. Köster, D. V, and S. Mayor. 2016. Cortical actin and the plasma membrane: inextricably intertwined. Curr. Opin. Cell Biol. 38: 81–89.

8. Murrell, M.P., and M.L. Gardel. 2012. F-actin buckling coordinates contractility and severing in a biomimetic actomyosin cortex. Proc. Natl. Acad. Sci. U. S. A. .

9. Vogel, S.K., F. Heinemann, G. Chwastek, and P. Schwille. 2013. The design of MACs (minimal actin cortices). Cytoskeleton. 70: 706–717.

10. Ideses, Y., A. Sonn-Segev, Y. Roichman, and A. Bernheim-Groswasser. 2013. Myosin II does it all: assembly, remodeling, and disassembly of actin networks are governed by myosin II activity. Soft Matter. 9: 7127.

11. Köster, D.V., K. Husain, E. Iljazi, A. Bhat, P. Bieling, R.D. Mullins, M. Rao, and S. Mayor. 2016. Actomyosin dynamics drive local membrane component organization in an in vitro active composite layer. Proc. Natl. Acad. Sci. 113: E1645–E1654.

12. Ortega Arroyo, J., D. Cole, and P. Kukura. 2016. Interferometric scattering microscopy and its combination with single-molecule fluorescence imaging. Nat. Protoc. 11: 617–633.

13. Bidone, T.C., W. Jung, D. Maruri, C. Borau, R.D. Kamm, T. Kim, M. Gardel, K. Kasza, C. Brangwynne, J. Liu, D. Weitz, M. Murrell, P. Oakes, M. Lenz, M. Gardel, E. Reichl, Y. Ren, M. Morphew, M. Delannoy, J. Effler, K. Girard, T. Bidone, H. Tang, D. Vavylonis, D. Laporte, N. Ojkic, D. Vavylonis, J. Wu, S. Tojkander, G. Gateva, P. Lappalainen, D. Burnette, S. Manley, P. Sengupta, R. Sougrat, M. Davidson, B. Kachar, P. Hotulainen, P. Lappalainen, D. Gordon, A. Bernheim-Groswasser, C. Keasar, O. Farago, Y. Inoue, S. Tsuda, K. Nakagawa, M. Hojo, T. Adachi, K. Popov, J. Komianos, G. Papoian, M. Lenz, M. Mak, M. Zaman, R. Kamm, T. Kim, P. Underhill, P. Doyle, G. Bell, T. Kim, H. Ennomani, G. Letort, C. Guérin, J.-L. Martiel, W. Cao, F. Nédélec, A.-C. Reymann, R. Boujemaa-Paterski, J.-L. Martiel, C. Guérin, W. Cao, H. Chin, W. Jung, M. Murrell, T. Kim, T. Erdmann, U. Schwarz, T. Erdmann, P. Albert, U. Schwarz, L. Cramer, M. Siebert, T. Mitchison, P. Oakes, Y. Beckham, J. Stricker, M. Gardel, C. Borau, T. Kim, T. Bidone, J. García-Aznar, R. Kamm, T. Kim, W. Hwang, R. Kamm, T. Kim, W. Hwang, H. Lee, et al. 2017. Morphological Transformation and Force Generation of Active Cytoskeletal Networks. PLOS Comput. Biol. 13: e1005277.

14. Albert, P.J., T. Erdmann, and U.S. Schwarz. 2014. Stochastic dynamics and mechanosensitivity of myosin II minifilaments. New J. Phys. 16.

15. Rastogi, K., M.S. Puliyakodan, V. Pandey, S. Nath, and R. Elangovan. 2016. Maximum limit to the number of myosin II motors participating in processive sliding of actin. Sci. Rep. 6: 32043.

16. Erdmann, T., K. Bartelheimer, and U.S. Schwarz. 2016. Sensitivity of small myosin II ensembles from different isoforms to mechanical load and ATP concentration. Phys. Rev. E. 94: 1–9.

17. Smith, D., F. Ziebert, D. Humphrey, C. Duggan, M. Steinbeck, W. Zimmermann, and J. Käs. 2007. Molecular motor-induced instabilities and cross linkers determine biopolymer organization. Biophys. J. 93: 4445–52.

18. Kruse, K., J.F. Joanny, F. Julicher, J. Prost, and K. Sekimoto. 2004. Asters , Vortices , and Rotating Spirals in Active Gels of Polar Filaments. Phys. Rev. Lett. 92: 1–4.

bioRxiv preprint doi: https://doi.org/10.1101/199778; this version posted October 17, 2017. The copyright holder for this preprint (which was not certified by peer review) is the author/funder, who has granted bioRxiv a license to display the preprint in perpetuity. It is made available under aCC-BY-NC-ND 4.0 International license.

19. Husain, K., and M. Rao. 2017. Emergent Structures in an Active Polar Fluid: Dynamics of Shape, Scattering, and Merger. Phys. Rev. Lett. 118: 1–5.

20. Keshavarz, M., H. Engelkamp, J. Xu, E. Braeken, M.B.J. Otten, H. Uji-I, E. Schwartz, M. Koepf, A. Vananroye, J. Vermant, R.J.M. Nolte, F. De Schryver, J.C. Maan, J. Hofkens, P.C.M. Christianen, and A.E. Rowan. 2016. Nanoscale study of polymer dynamics. ACS Nano. 10: 1434–1441.

21. Broedersz, C.P., M. Depken, N.Y. Yao, M.R. Pollak, D.A. Weitz, and F.C. Mackintosh. Cross-Link-Governed Dynamics of Biopolymer Networks. .

22. Alvarado, J., M. Sheinman, A. Sharma, F.C. MacKintosh, and G.H. Koenderink. 2013. Molecular motors robustly drive active gels to a critically connected state. Nat. Phys. 9: 1–7.

23. Kovács, M., J. Tóth, C. Hetényi, A. Málnási-Csizmadia, and J.R. Seller. 2004. Mechanism of blebbistatin inhibition of myosin II. J. Biol. Chem. 279: 35557–35563.

24. Billington, N., A. Wang, J. Mao, R.S. Adelstein, and J.R. Sellers. 2013. Characterization of three full-length human nonmuscle myosin II paralogs. J. Biol. Chem. 288: 33398–33410.

25. Gowrishankar, K., and M. Rao. 2015. Nonequilibrium phase transitions, fluctuations and correlations in an active contractile polar fluid. Soft Matter. 1201.3938.

26. Fritzsche, M., D. Li, H. Colin-York, V.T. Chang, E. Moeendarbary, J.H. Felce, E. Sezgin, G. Charras, E. Betzig, and C. Eggeling. 2017. Self-organizing actin patterns shape membrane architecture but not cell mechanics. Nat. Commun. 8: 14347.

27. Spudich, J.A., and S. Watt. 1971. The regulation of rabbit skeletal muscle contraction. I. Biochemical studies of the interaction of the tropomyosin-troponin complex with actin and the proteolytic fragments of myosin. J. Biol. Chem. 246: 4866–71.

28. Pollard, T.D. 1982. Myosin purification and characterization. Methods Cell Biol. 24: 333–71.

29. Ortega-Arroyo, J., and P. Kukura. 2012. Interferometric scattering microscopy (iSCAT): new frontiers in ultrafast and ultrasensitive optical microscopy. Phys. Chem. Chem. Phys. 14: 15625.

30. Cole, D., G. Young, A. Weigel, A. Sebesta, and P. Kukura. 2017. Label-Free Single-Molecule Imaging with Numerical-Aperture-Shaped Interferometric Scattering Microscopy. ACS Photonics. 4: 211–216.

31. Thielicke, W., and E.J. Stamhuis. 2014. PIVlab – Towards User-friendly, Affordable and Accurate Digital Particle Image Velocimetry in MATLAB. J. Open Res. Softw. 2.

32. Thielicke, W. 2014. The Flapping Flight of Birds - Analysis and Application.

bioRxiv preprint doi: https://doi.org/10.1101/199778; this version posted October 17, 2017. The copyright holder for this preprint (which was not certified by peer review) is the author/funder, who has granted bioRxiv a license to display the preprint in perpetuity. It is made available under aCC-BY-NC-ND 4.0 International license.

Figure 1, experimental setup: **A)** Diagram of the *in-vitro* system consisting of a supported lipid bilayer (orange), actin-membrane linker protein His10-KCK-EzrinABD (grey and red), actin filaments (green) and muscle myosin II filaments (blue). **B)** Example images of actin filaments (left) and myosin II filaments (right) recorded with the 445 nm laser iSCAT system; scale bar: 2 µm. **C)** Histogram depicting the interferometric contrast distribution along actin filaments (grey, N_{fil}=12, $N_{measure}$=562) and myosin II filaments (magenta, N_{fil}=5, $N_{measure}$=96).

Figure 2, single actin filament dynamics in an actin network: **A)** Dynamic features are visualized by subtracting the image sequence median from the raw images (left: raw image, right: median filtered); grey bar depicts the contrast range, scale bar: 5 µm. **B)** Histogram of the actin layer thickness in a typical experiment based on back ground subtracted, local interferometric contrast measurements divided by the contrast value of an individual actin filament (N=149). **C)** Image sequence depicting the dynamics of a single actin filament (red dashed line) inside an actin network; scale bar: 1 µm. **D)** Corresponding trajectory of the filament in (C) over time, small dots depict the tracked filament, bold dots its center of mass, color indicates time. **E)** Mean square displacement of the filament's center of mass shown in (D).

Figure 3, myosin II filament dynamics in the acto-myosin network at different ATP concentrations: **A)** Kymograph depicting myosin dynamics along static actin filaments generated from median filtered image sequences on the 635nm laser iSCAT setup. Black lines correspond to myosin II filaments that are moving along actin filament. **B)** Histogram of myosin II binding times to actin filaments at 100 µM ATP (N=6400). **C)** Histogram of myosin II binding times to actin filaments at 10 µM ATP (N=8000). **D-F)** Histograms of the myosin II filament velocities (D), run lengths (E) and frequency plot of run length vs binding time (F) extracted from myosin II filament kymographs at 100 µM ATP (N=1283). **G-I)** Histograms of the myosin II filament velocities (G), run lengths (H) and frequency plot of run length vs binding time (I) extracted from myosin II filament kymographs at 10 µM ATP (N=1840). Red lines depict fitted functions to describe the parameter distributions (single exponential function in (B,C, E and H), Gaussian fit in (D and G). Data displayed in (F and I) was limited to binding times of 10 s to focus on details in the short binding time regime.

Figure 4, dynamics of contracting acto-myosin networks: **A)** Image sequence depicting the dynamics of a membrane bound acto-myosin network acquired with the 445nm laser iSCAT setup; experimental conditions: [actin] = 250 nM, [capping protein] = 0.5 nM, [myosin II] = 30 nM, [ATP] = 50 µM; scale bar: 5 µm. **B)** Corresponding density-density correlation illustrating the network contraction in the rise of correlation length at later time points; the first peak at 200nm corresponds to single actin filaments; data was normalized by the maximum. **C)** Overlay of a snapshot of a contracting acto-myosin network (grey scale) and the vector flow field computed by particle image velocimetry (measured flow vectors: purple, interpolated vectors: cyan); bar 2 µm. **D)** Overlay of the same vector flow field and the corresponding divergence map indicating regions of contractility (purple, negative divergence) co-localizing with acto-myosin clusters. **E)** Histogram of the acto-myosin flow distribution computed by PIV of acto-myosin networks at 100 µM (red) and 10 µM (black) ATP. **F)** Example of an acto-myosin vortex visualized by a minimum projection of a 120 s image sequence (Video 5; scale bar 1 µm. **G)** Corresponding velocity map averaged over 120 s computed with PIV. **H)** Radial profile of the vortex velocity field shown in (G) (black:

bioRxiv preprint doi: https://doi.org/10.1101/199778; this version posted October 17, 2017. The copyright holder for this preprint (which was not certified by peer review) is the author/funder, who has granted bioRxiv a license to display the preprint in perpetuity. It is made available under aCC-BY-NC-ND 4.0 International license.

individual data points, red: averaged data). Experimental conditions in (C-H): [actin] = 300nM, [myosin II] = 80 nM.

Figure 5, myosin II filament attachment modes: Schematic depicting our proposed different modes of myosin II filament attachment to actin filaments: (i) attachment of one side of the myosin II filament to an actin filament corresponding to the short attachment time τ_{off1} and processive motion, (ii) attachment of both myosin II filament sides to the same actin filament resulting in the long attachment time τ_{off2} while moving processively and (iii) attachment of both myosin II filament sides to two different actin filaments leading to the long attachment time τ_{off2} and reduced processive motion.

Sup Figure 1, comparison of the 445nm and 635nm laser iSCAT set ups: A) Histogram of actin filament contrast measurements with the 445nm laser iSCAT setup, and fit of the first peak corresponding to the single actin filament signal. **B)** Histogram of actin filament contrast measurements with the 635nm laser iSCAT setup, and fit of the first peak corresponding to the single actin filament signal. **C)** Example image of an acto-myosin network with the 445 nm iSCAT setup highlighting myosin filaments (red arrows). **D)** Histogram of myosin II filament length measurements with the 445nm laser iSCAT setup and Gaussian fit (red line)(N=89). **E)** Example image of an acto-myosin network with the 635 nm iSCAT setup highlighting myosin II filaments (red arrows). **F)** Histogram of myosin II filament length measurements with the 635nm laser iSCAT setup and Gaussian fit (red line)(N=118).

Sup Figure 2, single actin filament dynamics: A) Image sequence of an actin filament landing on top of another imaged with the 445nm iSCAT setup. **B)** Corresponding measurement of the interferometric contrast of the region depicted by the white square in (A) showing a step-wise increase of the signal corresponding to the actin filament landing on top of another. **C)** Trajectory of a 4 µm long actin filament confined by the surrounding actin network, small dots depict the tracked filament, bold dots its center of mass, color indicates time. **D)** Mean square displacement of the filament's center of mass shown in (C) (blue), the diversion from the red line (depicting the expected MSD of a freely diffusing particle) at higher time scales indicates the confinement of the filament.

Video 1 Movie showing the increase in interferometric scattering when one actin filament lands on top of another depicted in SupFig 2A,B

Video 2 Movie showing the actin filament depicted in Fig 2C

Video 3 Movie showing myosin II filament motion along actin filaments (arrow heads) as analyzed in Fig3

Video 4 Movie showing the transition of the acto-myosin network from a homogeneous to a clustered state as analyzed in Fig 4A,B.

Video 5 Movie showing the myosin II filament dynamics forming a vortex analyzed in Fig 4F-H; interferometric scattering signal was inverted and images were converted into 8-bit format for analysis in PIVlab.

bioRxiv preprint doi: https://doi.org/10.1101/199778; this version posted October 17, 2017. The copyright holder for this preprint (which was not certified by peer review) is the author/funder, who has granted bioRxiv a license to display the preprint in perpetuity. It is made available under aCC-BY-NC-ND 4.0 International license.

Figure 1

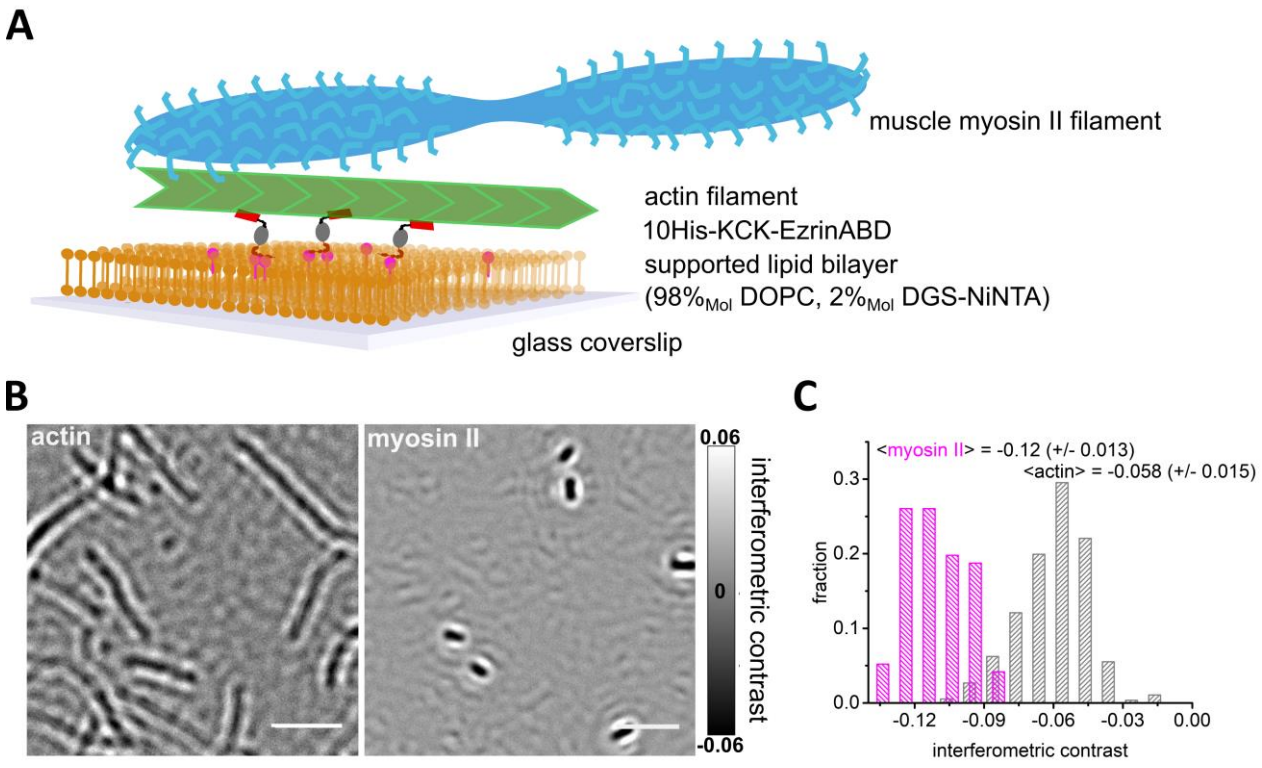

bioRxiv preprint doi: https://doi.org/10.1101/199778; this version posted October 17, 2017. The copyright holder for this preprint (which was not certified by peer review) is the author/funder, who has granted bioRxiv a license to display the preprint in perpetuity. It is made available under aCC-BY-NC-ND 4.0 International license.

Figure 2

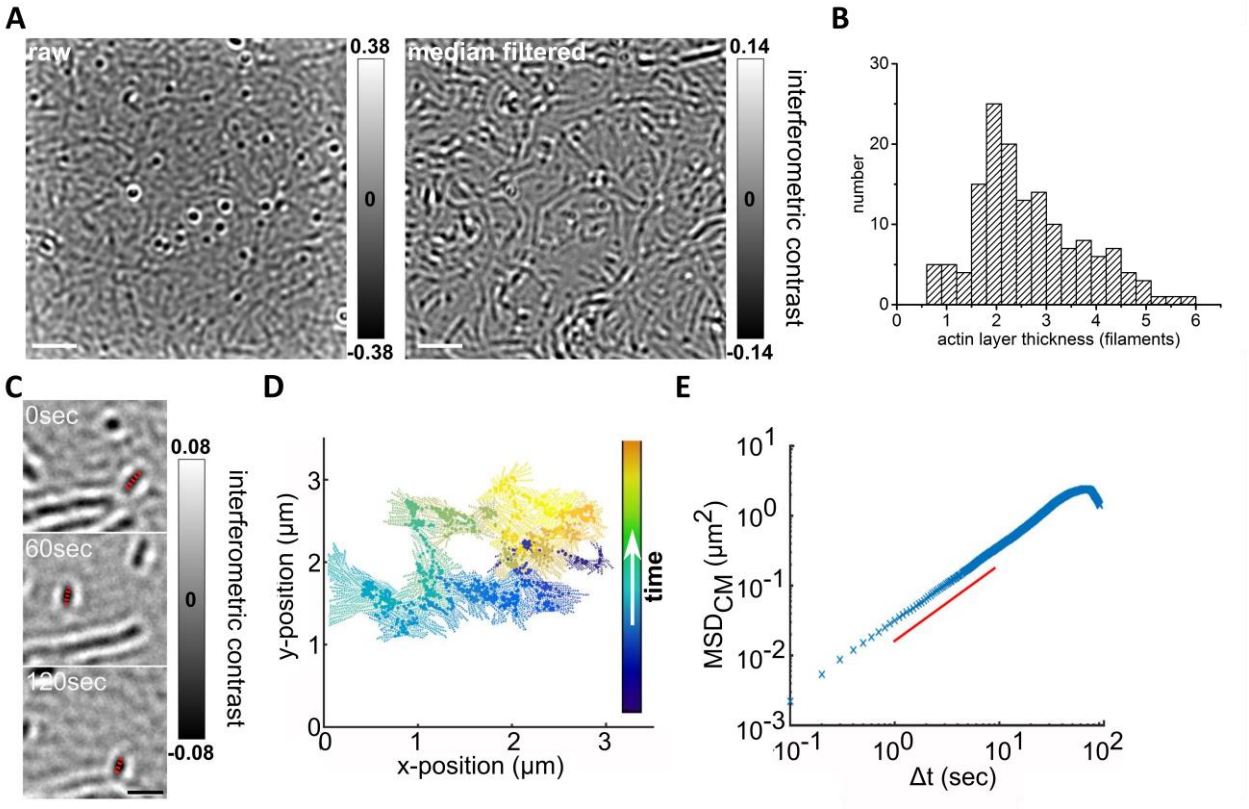

bioRxiv preprint doi: https://doi.org/10.1101/199778; this version posted October 17, 2017. The copyright holder for this preprint (which was not certified by peer review) is the author/funder, who has granted bioRxiv a license to display the preprint in perpetuity. It is made available under aCC-BY-NC-ND 4.0 International license.

Figure 3

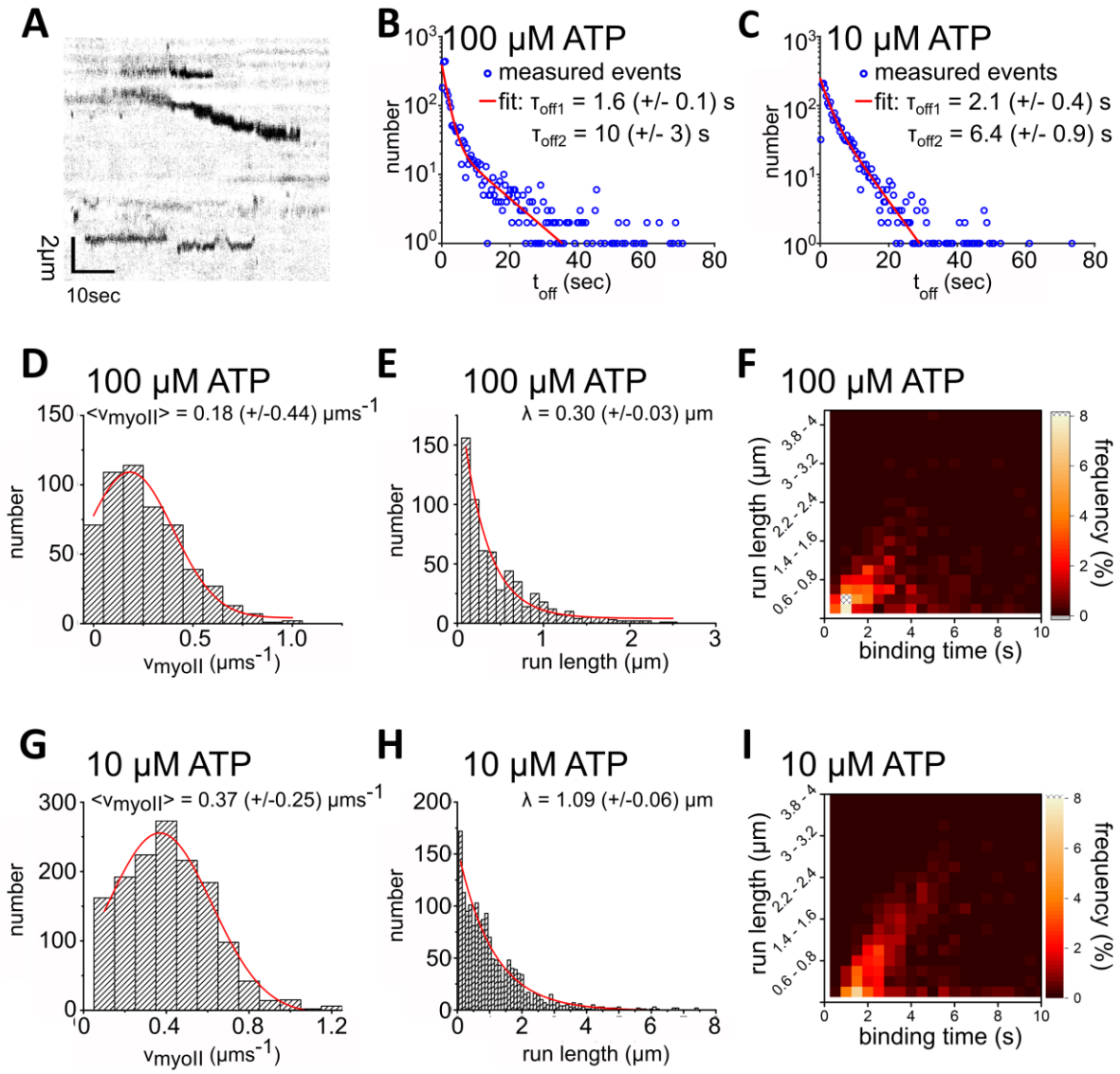

bioRxiv preprint doi: https://doi.org/10.1101/199778; this version posted October 17, 2017. The copyright holder for this preprint (which was not certified by peer review) is the author/funder, who has granted bioRxiv a license to display the preprint in perpetuity. It is made available under aCC-BY-NC-ND 4.0 International license.

Figure 4

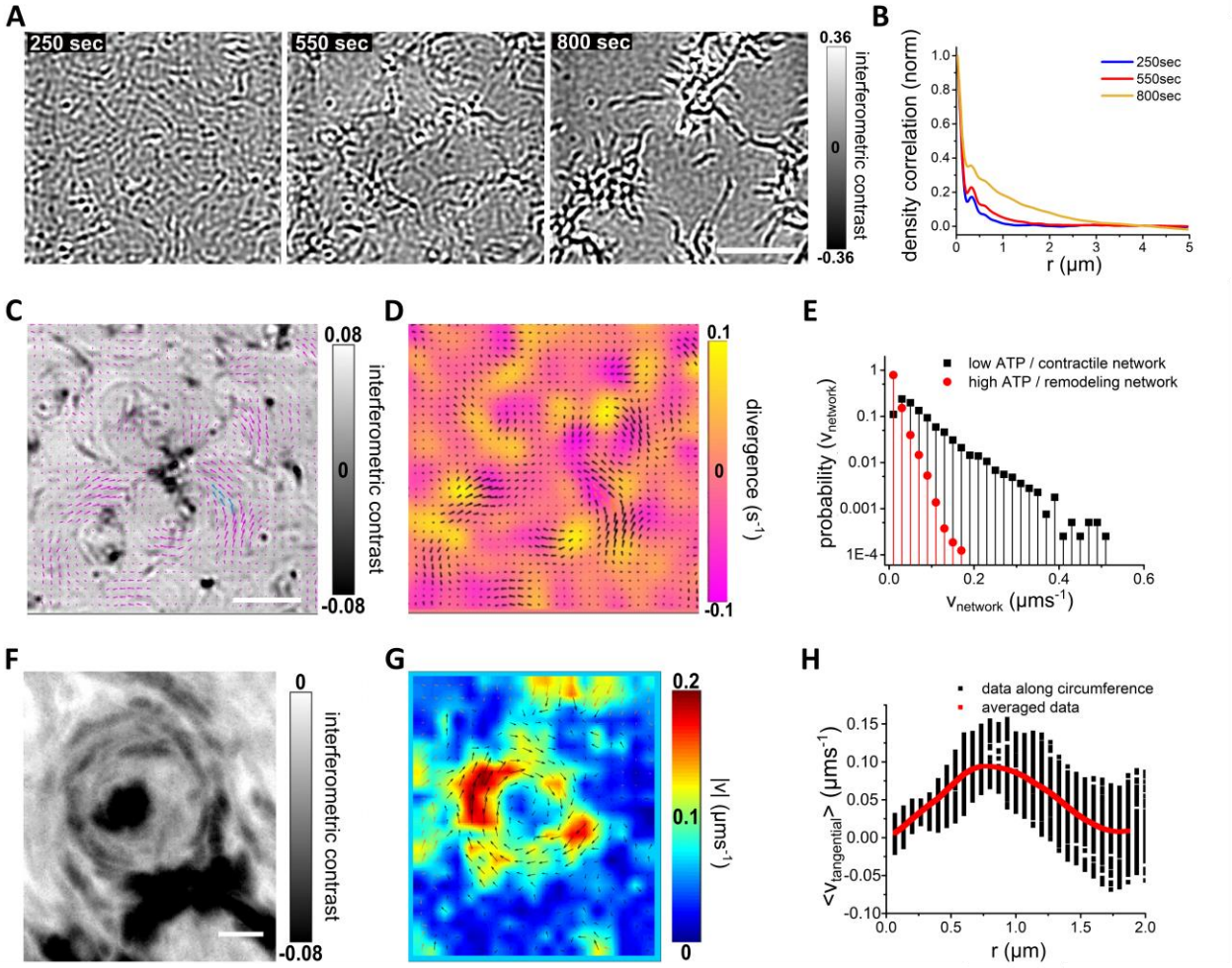

bioRxiv preprint doi: https://doi.org/10.1101/199778; this version posted October 17, 2017. The copyright holder for this preprint (which was not certified by peer review) is the author/funder, who has granted bioRxiv a license to display the preprint in perpetuity. It is made available under aCC-BY-NC-ND 4.0 International license.

Figure 5

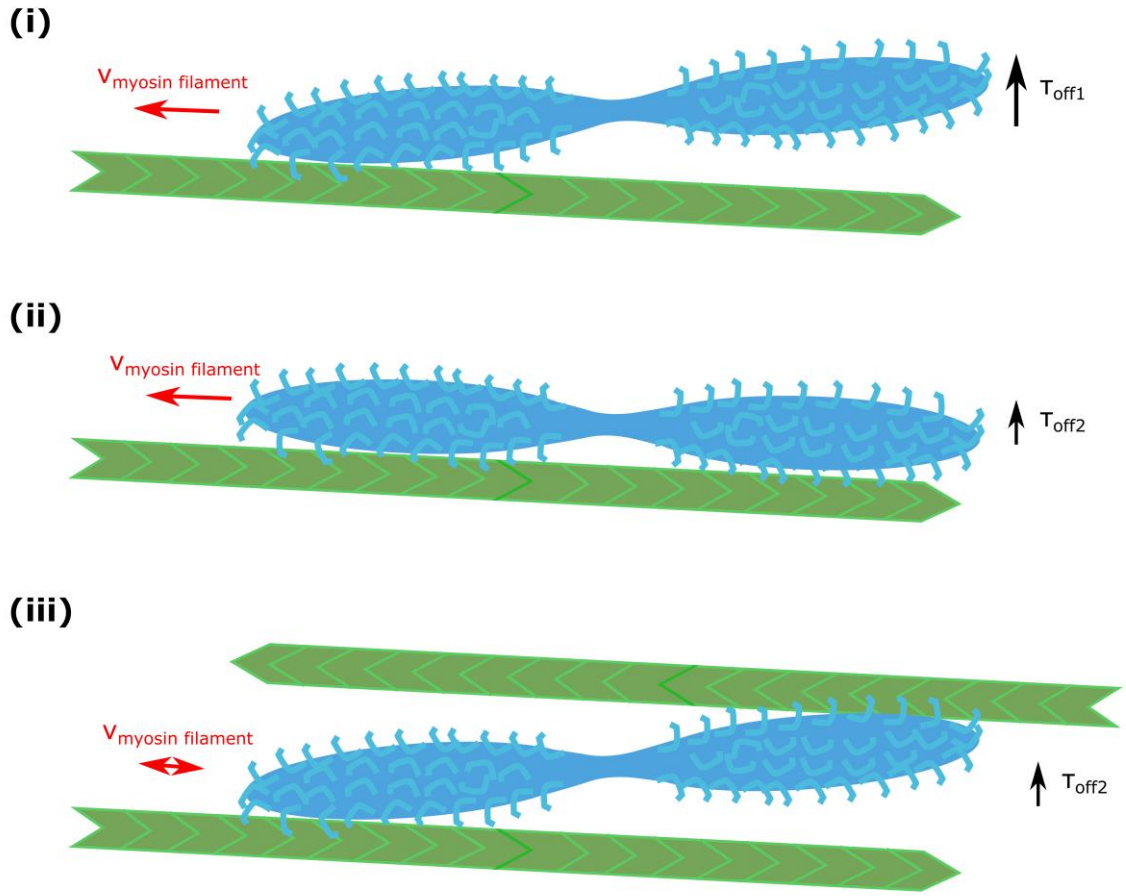

bioRxiv preprint doi: https://doi.org/10.1101/199778; this version posted October 17, 2017. The copyright holder for this preprint (which was not certified by peer review) is the author/funder, who has granted bioRxiv a license to display the preprint in perpetuity. It is made available under aCC-BY-NC-ND 4.0 International license.

Sup Figure 1

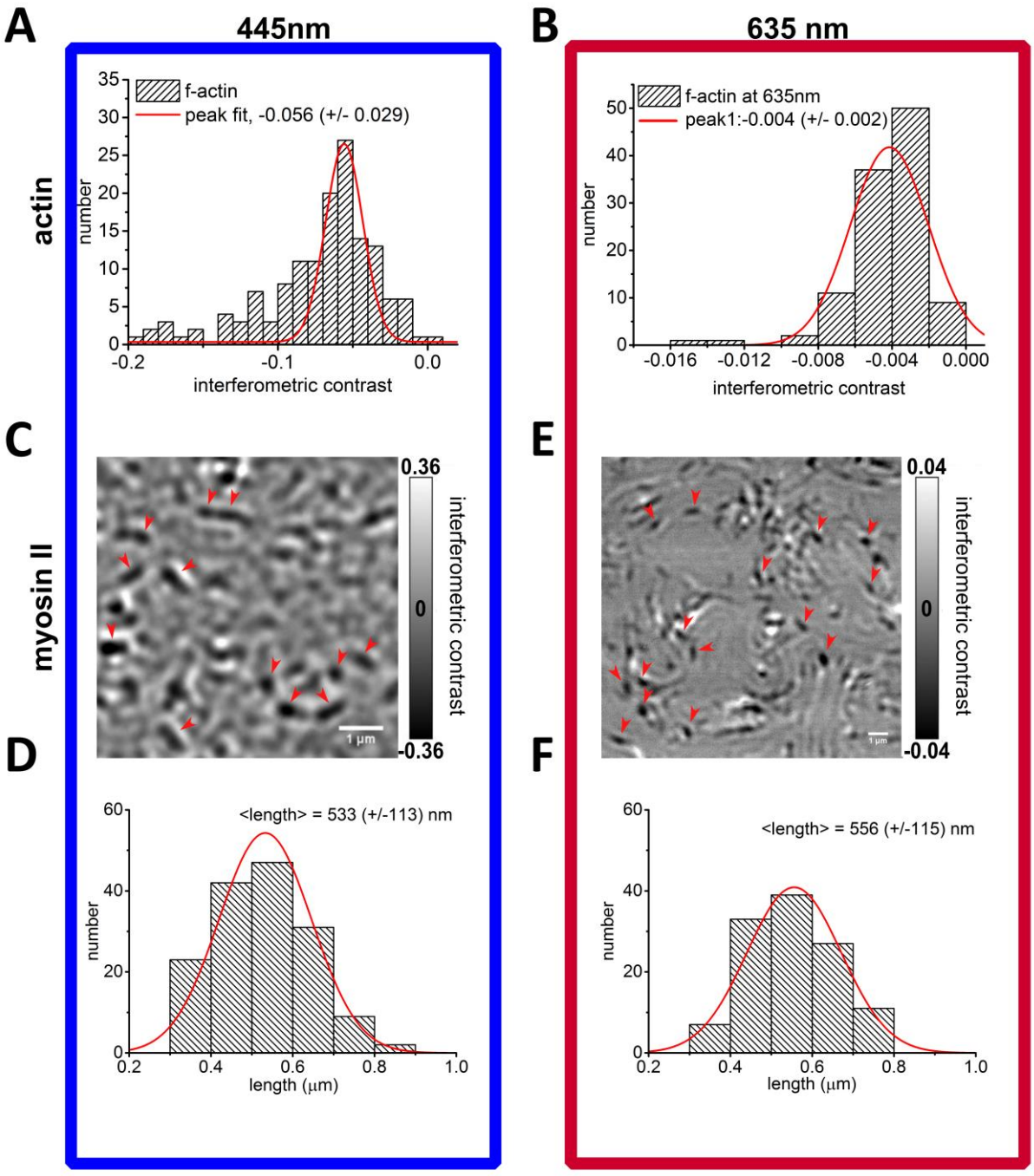

bioRxiv preprint doi: https://doi.org/10.1101/199778; this version posted October 17, 2017. The copyright holder for this preprint (which was not certified by peer review) is the author/funder, who has granted bioRxiv a license to display the preprint in perpetuity. It is made available under aCC-BY-NC-ND 4.0 International license.
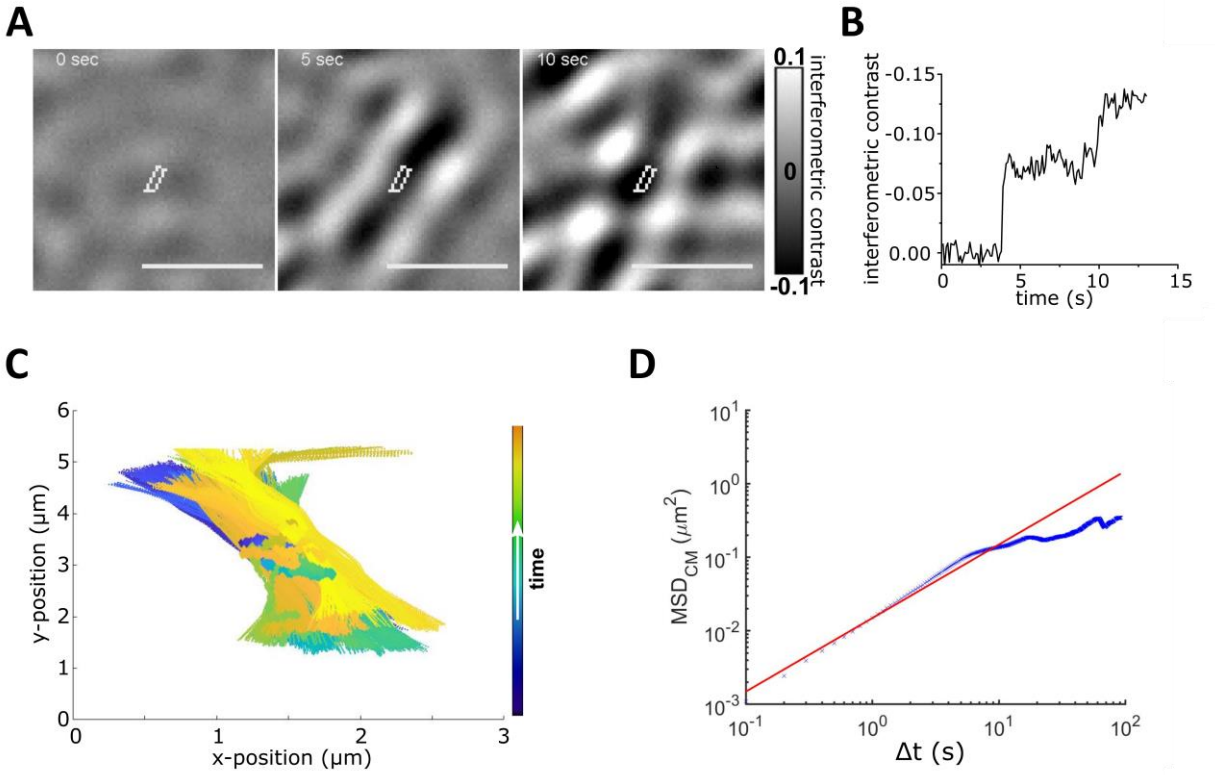
Sup Figure 2